Validation of E-region Model Electron Density Profiles with AURIC utilizing High-Resolution Cross Sections

MD Nazmus Sakib[1], Emmaris Soto[2], Erdal Yiğit[1], J. Scott Evans[2], R. R Meier[1]

[1]Department of Physics and Astronomy, Space Weather Lab, George Mason University, Fairfax, VA 22030, USA

[2]Computational Physics Inc., 8001 Braddock Rd, Suite 210, Springfield,VA 22151, USA

Key Points:

- AURIC simulations are updated utilizing high-resolution photoionization and photoabsorption cross sections and scaled solar spectra.
- Multi instrument observations have been used to compare electron density profiles with AURIC E-region high-resolution modeling efforts.
- New high-resolution calculations show improvement in the E-region electron density calculation by producing more ionization.

Corresponding author: Md Nazmus Sakib, msakib@gmu.edu

Abstract

E-region models have traditionally underestimated the ionospheric electron density. We believe that this deficiency can be remedied by using high-resolution photoabsorption and photoionization cross sections in the models. Deep dips in the cross sections allow solar radiation to penetrate deeper into the E-region producing additional ionization. To validate our concept, we perform a study of model electron density profiles (EDPs) calculated using the Atmospheric Ultraviolet Radiance Integrated Code (AURIC; D. Strickland et al. (1999)) in the E-region of the terrestrial ionosphere. We compare AURIC model outputs using new high-resolution photoionization and photoabsorption cross sections, and solar spectral irradiances during low solar activity with incoherent scatter radar (ISR) measurements from the Arecibo and Millstone Hills observatories, COSMIC-1 observations, and outputs from empirical models (IRI-2016 and FIRI-2018). AURIC results utilizing the new high-resolution cross sections reveal a significant difference to model outputs calculated with the low-resolution cross sections currently used. Analysis of AURIC EDPs using the new high-resolution data indicate fair agreement with ISR measurements obtained at various times at Arecibo but very good agreement with Millstone Hills ISR observations from ~ 96 km to 140 km. However, discrepancies in the altitude of the E-region peak persist. High-resolution AURIC calculations are in agreement with COSMIC-1 observations and IRI-2016 model outputs between ~ 105 km and 140 km while FIRI-2018 outputs underestimate the EDP in this region. Overall, AURIC modeling shows increased E-region electron densities when utilizing high-resolution cross sections and high-resolution solar irradiances, and are likely to be the key to resolving the long standing data-model discrepancies.

1 Introduction

The E-region ionosphere is a natural plasma laboratory where neutral processes play an important role in shaping the ionosphere. While photochemical processes are crucial in establishing the structure of the E-region (Chu et al., 2009), dynamical processes, such as tidal and gravity wave propagation, and dissipation modulate the underlying neutral structures (Yiğit & Medvedev, 2015). These processes form the terrestrial ionosphere that extends from ~ 60 km up to ~ 1000 km above the surface of the Earth and contains multiple distinct regions of charged particles (D, E, and F regions), characterized by the variation of the electron density as a function of height. Each of these layers has its own density maximum at a certain height.

Although the ionospheric E-region was the first to be discovered (E. V. Appleton & Barnett, 1925), the details of the physical and chemical processes governing the mean and variable structure of this region are still not well understood. Thus, validation of E-region electron density modeling and better characterization of the altitude variations of plasma density in this region is extremely important. One complexity of the E-region ionosphere, which coincides in altitude with the lower thermosphere, is that it is influenced by processes from below and above (Yiğit et al., 2016; Ward et al., 2021; Shiokawa & Georgieva, 2021). Various photochemical processes are predominant in the E-region and it is often challenging to decouple the sources of variability in observations. Therefore, idealized numerical models, such as the Atmospheric Ultraviolet Radiance Integrated Code (AURIC; D. Strickland et al. (1999)), are a powerful tool to isolate sources of variability.

The primary objective of this paper is to validate the latest version of AURIC, by comparing E-region model electron density profiles (EDPs) with observations from both ground-based (e.g., radars) and space-borne instruments (e.g., satellites) along with other existing empirical models, and to study the E-region ionospheric structure and variability. Previously, D. Strickland et al. (1999) compared the initial version of AURIC with a number of observations by rockets and satellite measurements in terms of photoelectron flux, dayglow and ion density distribution measured by AE-E satellite photoelectron flux data, FUV and MUV dayglow rocket data, AE-E ion-mass spectrometry data, respectively. These studies showed reasonable agreement between the data and model. For the first time, in this study, we utilize EDPs as a probe to compare outputs from high resolution AURIC calculations with state-of-the-art ground-based and space-borne observations.

2 Brief Description of the Instruments and Models

2.1 Instrument Description

2.1.1 Arecibo ISR

The Arecibo incoherent scatter radar (ISR) is situated at Arecibo, Puerto Rico ($18.44°$N, $293.2°$E) and is very well known in the field of ionospheric and astrophysics research. In this study, we particularly selected data described in the work by Sojka et al. (2014), which is a radar campaign to understand the low latitude E-region EDPs on February 9, 2012. The local time at Arecibo is given in 'Atlantic Standard Time' (AST), which is 4 hours behind of Universal Time Coordinate (UTC) i.e., UTC = AST + 4.

2.1.2 Millstone Hills ISR

The ISR at Millstone Hills (42.61°N, 288.5°E) is another well known ground based radar which is used in observing mid latitude ionospheric EDPs (e.g., Lei et al., 2005; Zhang et al., 2011; Yan et al., 2020, and references therein). Millstone Hills ISR observes ionospheric EDPs using two different techniques: alternating code (AC) and single pulse (SP). While SP provides data at a vertical resolution of about 18 km, AC provides data at a resolution of about 4.5 km. Our study utilizing AC data contains electron density information below 400 km (Lei et al., 2007). We downloaded data from the MIT Madrigal Database for February 16, 2012, which has similar geomagnetic and solar condition in comparison with Arecibo ISR campaign data on February 9, 2012 (see section 3 for more detail).

2.1.3 COSMIC-1 GPS Radio Occultation (RO)

The Constellation Observing System for Meteorology Ionosphere and Climate, also called COSMIC-1 (USA) or Formosa Satellite Mission-3 - FORMOSAT-3 (Taiwan) (Anthes et al., 2008), consists of 6 small equidistant satellites forming a constellation in a circular orbit at around 800 km from the surface of the Earth (Chu et al., 2009). This system of satellites was successfully launched on April 15, 2006 and retired in 2020. The University Corporation for Atmospheric Research - COSMIC Data Analysis and Archive Center (UCAR-CDAAC) provides COSMIC-1 level 2 ionospheric profile data, reprocessed in 2013 and 2021. Based on an inversion technique to get electron density profiles from radio signal refractivity, there are two kinds of COSMIC-1 radio occultation profiles, namely “ion-profile” and “iga-profile”. Ion profiles data are the refracted signals of occultations measurements inverted using the standard Abel inversion method which assumes spherical symmetry. The latter one is recently updated, removing the spherical symmetry assumption, and considering the horizontal gradient of atmospheric constituents. All of these profiles can be used for various scientific purposes, but our study will use more improved iga profiles as these profiles are expected to produce less error in E-region electron density measurement. Any typical ion profile or iga profile contains vertical electron density, total vertical electron content, mean sea level altitude of observed profiles ($\sim$ 50 km to $\sim$ 800 km), occultation azimuth angle and perigee point geolocations (i.e., latitude and longitude) of the observation (top to bottom).

McGranaghan et al. (2015) compared a set of COSMIC-1 RO data with an improved version of GLOW (an ionospheric numerical model) (Solomon et al., 1988; Bailey et al., 2002) which

calculates electron transport and chemical reactions with optimized time (GLOWfast) along with the older version (GLOWfull) in terms of electron number density vertical profiles and found reasonable agreement at the bottom side of the E-region, though their analysis also showed discrepancy (less than factor of two) in upper E-region. None of the COSMIC-1 and GLOW model comparisons produce agreement in terms of E-region peak height (shifted by ~ 5 to ~ 10 km).

Prior to that, Sheng et al. (2014) compared COSMIC electron density profiles with ground based ISR focusing on the F-region and found profiles during summer time are more reliable though the electron density profiles extend down to around 100 km.

The systematic and observational error of radio occultations by COSMIC satellites is well explained in Lei et al. (2007). That paper compared COSMIC individual electron density vertical profiles with Millstone Hills and Jicamarca radar observations in similar geolocations. For the topside ionosphere, COSMIC data is more suitable to study as horizontal gradient has minimum effect on EDPs (Lai et al., 2013). However, this study will use COSMIC-1 EDPs (iga format) at E-region which is more improved and considers horizontal gradient effects (Pedatella et al., 2015) to compare with our model AURIC.

2.2 Model Description

2.2.1 AURIC

AURIC is an integrated physics-based model developed by Computational Physics Inc. to calculate the the upper atmospheric spectral radiance (airglow) from the FUV to near infrared, including aerosol and Rayleigh scattering of sunlight and moonlight from the middle and lower atmosphere, and densities of species that are chemically active above 100 km from the surface of the Earth (D. Strickland et al., 1999). The term 'integrated' refers to the combination of a UV radiance model with Air Force model MODTRAN (Berk et al., 1987). Details about the development of AURIC can be found in previous works by Link et al. (1993); D. J. Strickland et al. (1996); Majeed and Strickland (1997, and references there in). AURIC requires direct user inputs including date and universal coordinate time (UTC), geographic latitude and longitude, observer altitude and look angle and spectral interval and resolution. Derived user inputs are geomagnetic latitude and longitude, dip angle, solar zenith angle, solar local time (LST), F10.7 (current and 81-day average) and AP history. The first version of AURIC used generated file inputs such as model neutral atmosphere by Mass Spectrometer and Incoherent Scatter data thermosphere model (MSIS-E-90) (Hedin, 1991) and SHARC and MODTRAN Merged (SAMM) (Sharma et

al., 1996) of N_2, O_2, O, N, NO, O_3 species, model ionosphere by Fully Analytic Ionospheric Model (FAIM; Anderson et al., 1989), geomagnetic field by corrected geomagnetic coordinates (GEO-CGM; Gustafsson et al., 1992), and incident solar EUV spectrum by Hinteregger et al. (1981). In that version, database files and encoded data inputs are photoabsorption and photoionization cross sections (Conway, 1988; Bell & Stafford, 1992), solar reference EUV spectrum (Hinteregger et al., 1981), electron impact cross sections, chemical rate coefficients, molecular transition arrays, and molecular population distributions. For convenience, we refer to the low-resolution AURIC cross sections as "Conway", even though his is a compilation from many sources. The Conway report can be accessed at Conway (1988). The current version of AURIC has been modified with a new high-resolution calculation of photoionization and photoabsorption cross sections for O updated from Meier et al. (2007) and N_2 (Soto et al., 2023) along with new high-resolution calculations of solar spectral irradiance (Warren, 2005). **Our primary interest is to determine and report if model calculations using new high resolution solar spectral irradiances and photoionization and photoabsorption cross sections resolve prior data-model discrepancies with E-region EDPs**.

2.2.2 IRI-2016

The International Reference Ionosphere (IRI) is an empirical model widely used for ionospheric reference initiated jointly by the Committee on Space Research (COSPAR) and the International Union of Radio Science (URSI) since the late sixties for the most important plasma parameters in Earth's ionosphere (Bilitza et al., 1993). An updated review of the model can be found in the work by Bilitza et al. (2022). The first widely circulated edition was IRI-78 (Rawer et al., 1978); however, our study utilizes the latest version IRI-2016 (Bilitza et al., 2017). This new version of IRI takes additional input of peak electron density (N_mF2) at F2 height (h_mF2), and an improved description of ion composition at high and low solar activity based on data from satellites such as C/NOFS-CINDI. Other input parameters of this model are solar indices F10.7 radio flux (daily, 81-days, and 12-months running mean), sunspot number R_z (13-months running mean), Ionospheric index such as ionosonde-based IG index (12-months running mean) (Brown et al., 2018) and geomagnetic index such as Ap index (daily average, 3-hour planetary). The web-based version of this model can predict altitude profiles of electron density, electron temperature, ion temperature, major ion composition and total electron content (TEC) from 50 km to 2000 km for those specific inputs.

2.2.3 FIRI-2018

Our study utilizes another empirical model at lower altitudes in the ionosphere called Faraday-International Reference Ionosphere (FIRI)-2018 (Friedrich et al., 2018) originally published in 2001 as a semi-empirical model (Friedrich & Torkar, 2001). This is a specialized IRI model for the non-auroral ionosphere valid for altitudes above 60 km up to 150 km. One can utilize the python based version of this model varying four input parameters such as day (Julian day of the year from 1-365), solar zenith angle (0-130°), latitude (0-60°) and solar radio flux F10.7 (75-200 solar flux unit).

3 Geomagnetic conditions on the observational days

Figure 1 shows a time plot of geomagnetic and solar EUV activity for February (29 days) in 2012. The vertical solid and dotted red lines in Figure 1 identify February 9 and February 16, respectively, which correspond to the data analyzed here. For first four panels, we utilize data provided by the Adolf-Schmidt-Observatory for Geomagnetism in Niemegk operated by the GFZ German Research Center for Geosciences (Matzka et al., 2021). The top two panels (a and b) show the planetary Kp index (three-hourly equivalent) at 12:00-15:00 UT and daily equivalent planetary Ap index, which is the arithmetic mean of three-hour equivalent Ap values of the whole day calculated from Kp. History and a detailed description of these geomagnetic indices can also be found in Bartels (1949, 1957); Matzka et al. (2021, and references therein). Local noon time observed 10.7 cm solar radio flux ($F_{10.7}$) is presented in Figure 1(c) in the unit of s.f.u. (= 10^{-22} W m^{-2} Hz^{-1}), using a dataset provided by the Dominion Radio Astrophysical Observatory and National Research Council, Canada (Tapping, 2013). Figure 1(d) shows the individual international sunspot number (SN) provided by the Royal Observatory of Belgium in Brussels. Descriptions of the SN series based on all the corrections by different observations are given in the work by Clette and Lefèvre (2016). Data source for GOES X-ray (Figure 1(e)) is NOAA Space Weather Prediction Center (SWPC) and we have utilized GOES-15 level 2 X-ray sensor 1-minute irradiance average for the entire month of February 2012. On the other hand, source of hourly equatorial Dst index data (Figure 1(f)) is World Data Center for Geomagnetism, Kyoto, Japan.

4 Analysis and Results

In this study, we investigate the impact on E-region electron densities of new photoionization and photoabsorption "high-resolution" cross sections used in the AURIC model (Soto et al., 2023), along with model output using the "low-resolution" cross sections from Conway (1988).

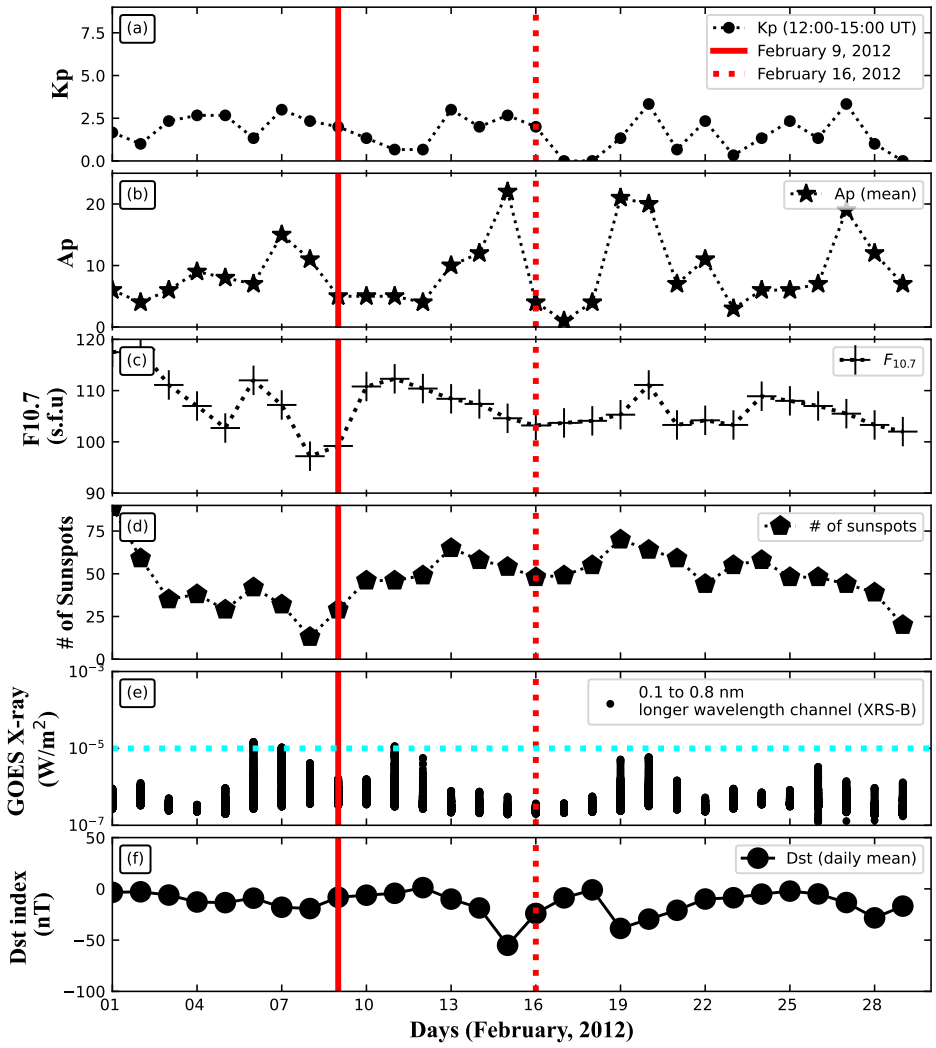

Figure 1. Geomagnetic index and solar condition for the month of February 2012 (29 days). Panel a and b : Kp (dot symbol) and Ap (star symbol) index. Panel c and d : F10.7 (plus symbol) and sunspot number (pentagon symbol). Panel e: GOES-15 level 2 X-ray sensor 1-minute irradiance daily average. Cyan horizontal line indicates the lower limit of solar M-class flare. Panel f: Disturbance storm time (Dst) index. February 9, 2012 is represented by the vertical red solid line and February 16, 2012 by the vertical red dotted line.

We carry out model simulations by AURIC for February 9 and 16, 2012, which are consistent with observational data by Arecibo and Millstone Hills ISRs. In a companion paper, Soto et al. (2023) describe the details of the new high-resolution cross sections and solar spectral irradiance. That paper shows that the implementation of new high-resolution inputs in the model increases the total photoionization rate (133%) in the E-region. Using the same high-resolution photoionization and photoabsorption cross sections and solar spectral irradiances, we validate AURIC model outputs with state-of-the-art remote sensing observations.

4.1 Comparison between AURIC and Arecibo ISR

Figure 2 shows three different "hourly" mean EDPs and corresponding individual EDPs observed by Arecibo ISR on 9 February 2012 during daytime conditions. The whole data set consists of 82 EDPs from 8:03 Hr AST to 16:00 Hr AST from 90 km to $\sim$ 400 km.

The morning profile represents Arecibo observations at 8-9 Hr AST or 12-13 Hr UTC. Similarly, the noon profile (12-13 AST) corresponds to 16-17 Hr UTC and afternoon profile (15-16 AST) corresponds to 19-20 Hr UTC. These hourly binned mean EDPs show local solar time variation with maximum ionization at noon in terms of peak electron density at the E-region (N_mE). The shaded region around hourly mean EDPs in Figure 2 represent the 1-σ standard deviation of measurements at each altitude step. As expected theoretically, the maximum ionization occurs around local noon. Additionally, hourly mean EDPs remain almost invariant from 90 km to 95 km (at $\sim$ 96 km, the noon mean EDP shows a 36% discrepancy with the morning mean EDP and 31% discrepancy with the afternoon mean EDP) and more distinctive above $\sim$ 100 km (at $\sim$ 102 km, the noon mean EDP shows a 74% discrepancy with the morning mean EDP and 12% discrepancy with the afternoon mean EDP).

Arecibo observations show peak E-region EDP heights (h_mE) at $\sim$ 114 km for morning, $\sim$ 108 km for noon, and $\sim$ 106 km for afternoon times. At these altitudes, the mean N_mE values are $\sim 9.29 \pm 1.01 \times 10^{10}$ m^{-3}, $\sim 1.53 \pm 0.02 \times 10^{11}$ m^{-3} and $\sim 1.21 \pm 0.09 \times 10^{11}$ m^{-3}, respectively.

To compare these real time Arecibo observations with AURIC calculated electron density profiles, we assumed electrical quasi-neutrality, i.e., the number density of positive ions is equal to the number density of electrons, or $n_e = \sum_i n_i$, where i represents the number of positive ion species (Prölss, 2012). We summed up five major 'long lived' positive ions including NO^+, O_2^+, O^+, N^+, and N_2^+ to construct the electron density altitude profiles.

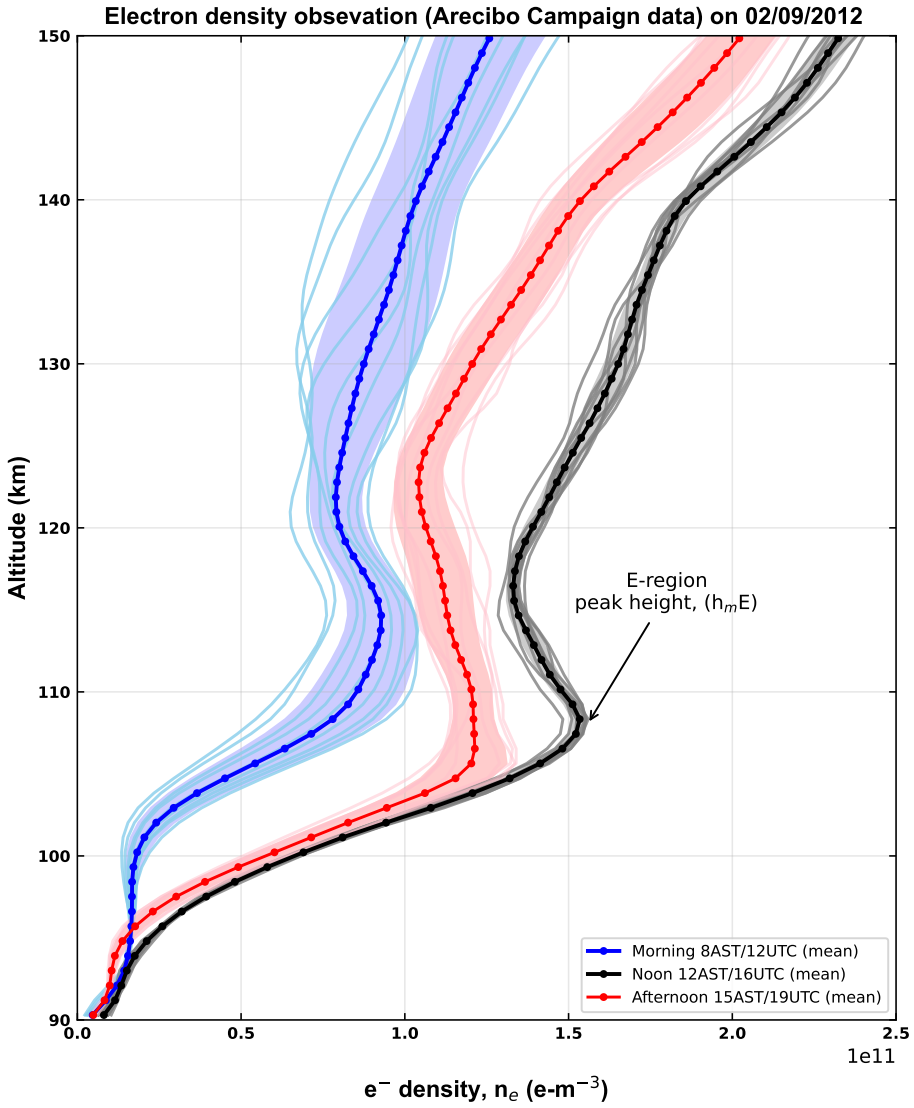

Figure 2. Arecibo ISR measured sunlit atmosphere hourly mean electron density as a function of altitude at 8:00 (blue), 12:00 (black) and 15:00 (red) AST observed by Arecibo ISR (18.44°N, −66.67°W) on February 9, 2012 . Light blue, grey and pink profiles represent the raw observations within those hours. Shaded region in each profile shows 1-σ standard deviation that represents natural variability of the data.

As mentioned earlier, to understand the impact of high-resolution cross sections and solar spectral irradiances in model simulations, we used both the low-resolution cross sections from the Conway (1988) compilation and the newly calculated high-resolution cross sections as inputs to the model. Additionally, this study utilizes a new high-resolution solar EUV spectrum constructed by scaling the high-resolution spectrum data delivered by H. Warren and Sherry Chhabra for Feb 9 and Feb 16, 2012. We put the solar spectrum on an absolute irradiance scale using a model of the solar EUV spectral irradiance (Lean et al., 2011) updated with the latest data (Lean et al., 2020; Woods et al., 2012; Lean et al., 2003) to compute solar spectral irradiance (see companion paper by Soto et al., 2023).

Two different AURIC runs can be seen in each panel of Figure 3. Curves labeled 'low-resolution' refer to model simulations based on low-resolution Conway cross sections with a low-resolution solar spectrum and 'high-resolution' refers to model results using high-resolution cross section data with high-resolution solar spectrum. The high-resolution cross sections have a resolution of 0.001 nm while the low-resolution cross sections have a resolution of 0.05 nm below 10 nm and 0.1 nm above 10 nm. The original resolution of the delivered solar spectrum is 0.001 nm; however, in order to run AURIC for the low-resolution case we bin the high-resolution spectrum onto the low-resolution AURIC grid (see Soto et al., 2023, for more detail).

Non-auroral E-region electron density profile can be characterized by a modest peak (N_mE) located near $\sim 105{-}110$ km, which is a function of solar radiation, atmospheric composition, and atmospheric temperature (Solomon, 2006). Our work partially focuses on a comparison study of peak values of EDPs and heights of the peak EDPs (h_mE) between data and model to gain insight about data-model discrepancies given the high uncertainty of the peak values and heights. A derivative parameter, the E-region critical frequency (f_oE), is directly proportional to peak electron density (N_mE), and is also a conventional measure in the ionospheric physics community (see Appendix B for more detail). Our comparison is conducted by calculating the relative percent differences of these values between data and model. A quantitative comparison between Arecibo observations and AURIC runs is shown in Table 1 where the relative percentage difference (denoted by $\Delta_{rel}(\%)$) of AURIC calculations with respect to Arecibo observations is calculated by,

$$\Delta_{rel} = \frac{|AURIC - Arecibo|}{Arecibo} * 100\% \tag{1}$$

Specifically, during morning and in terms of N_mE, the mean absolute difference between the low-resolution AURIC ion production rate and the Arecibo ISR data is $\sim 32\%$ whereas the

mean absolute difference for the high-resolution model output is $\sim 33\%$, as can be seen from from Figure 3(a) and Table 1(a). Clearly, the AURIC morning time high-resolution EDP is shifted towards real time observation than the low-resolution AURIC run. However, the high resolution cross sections do not preserve the characteristic E-region local maxima in between ~ 105 km and $\sim$ 110 km during a sunlit condition, in contrast with low-resolution AURIC runs. Therefore, we used the observed h_mE to estimate the AURIC N_mE for comparison with the observed N_mE. Tables 1(b) and 1(c) likewise show values of N_mE, h_mE, f_oE, and the corresponding discrepancy between data and model for noon and afternoon times, respectively.

During noon time (see Figure 3(b)), the Arecibo observed N_mE (f_oE) shows $\sim 13(\sim 7)\%$ and $\sim 18(\sim 9)\%$ discrepancy with respect to the high-resolution and low-resolution model calculations. At afternoon time (see Figure 3(c)), Arecibo ISR observation and AURIC model discrepancy is $\sim 4(2)\%$ and $\sim 6(3)\%$, for high and low-resolution runs, respectively.

The low-resolution AURIC results agree better with data during the afternoon time (see Figure 3(c)). In order to investigate the reason for this, we checked multiple factors, such as the impact of changing the photoionization and photoabsorption cross section magnitude, difference of photoabsorption cross section, volume production rate, and the neutral atmospheric input in the model. We reached the conclusion that the E-region electron density peak can be better reproduced provided that O_2 high resolution cross sections are implemented as well. Figure S1 in the Supporting Information illustrates the strong dependence of the lower EDP peak with the O_2^+ (X) ionization rate as a function of altitude, and to a lesser extent the dependence on the O^+ (^4S_o) ionization rate. The large contributions from these states, particularly the O_2^+ (X) state, between approximately 105-130 km reflect an increase in the transmission dictated by the structure in the high-resolution N_2 photoabsorption cross section. Incorporation of high-resolution O_2 photoabsorption and photoionization cross sections may further impact the ionization rate magnitude and peak, and thus shape of the EDP. Additionally, several other missing physical processes in the model, such as lack of diffusion mechanism, atmospheric extinction at E-layer specially absorption of solar X-rays and EUV at this altitude, and as a consequence secondary ionization by energetic photoelectrons, or other dynamical processes, such as ion drifts and ion-neutral interactions could produce the similarity with the low-resolution results. Using high-resolution physics in the model could potentially reveal or highlight the importance of the above mentioned processes that are currently not accounted for. Overall, the high-resolution AURIC output produces more ionization at E-region than the previously employed low-resolution cross sections of AURIC runs.

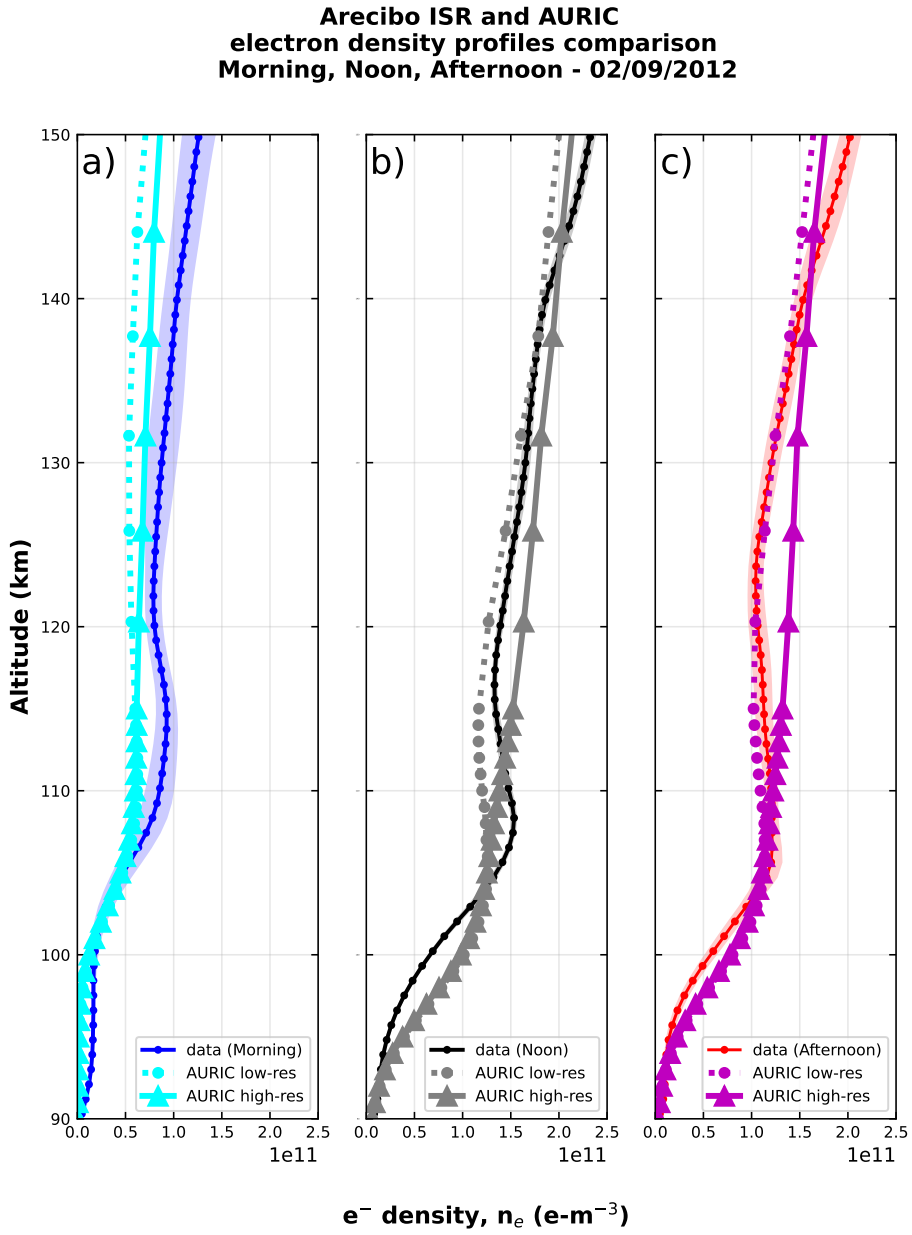

Figure 3. Daytime electron density comparison between data and model. Electron density as a function of altitude calculated by AURIC at a) (right panel) 8 AST/12 UTC (cyan), b) (middle panel) 12 AST/16 UTC (grey) and c) (left panel) 15 AST/19 UTC (majenta) with two different sets of cross section - low-resolution (circular dashed line) and high-resolution (triangular solid line) overlapped with Arecibo ISR measured EDPs (e- m^{-3}) at the same time. Blue, black, and red profiles represents Arecibo ISR observations at local solar time morning, noon, and afternoon, respectively on that day (same as Figure 2). See text for more detail.

Table 1. Quantitative Comparison between Arecibo ISR observation and AURIC

Morning[a]	N_mE (e^-/m^3)	h_mE (km)	f_oE (MHz)	$\Delta_{rel}(N_mE)$ (%)	$\Delta_{rel}(h_mE)$ (%)	$\Delta_{rel}(f_oE)$ (%)
Arecibo	9.28E+10	114.66	2.74	0.00	0.00	0.00
Low-resolution	6.23E+10	112.00	2.25	32.85	2.32	18.05
High-resolution	6.16E+10	114.00	2.23	33.59	0.58	18.51

[a] at 12 UTC

Noon[b]	N_mE	h_mE	f_oE	$\Delta_{rel}(N_mE)$	$\Delta_{rel}(h_mE)$	$\Delta_{rel}(f_oE)$
Arecibo	1.53E+11	108.34	3.53	0.00	0.00	0.00
Low-resolution	1.26E+11	105.00	3.20	17.81	3.08	9.34
High-resolution	1.33E+11	108.00	3.28	13.62	0.31	7.06

[b] at 16 UTC

Afternoon[c]	N_mE	h_mE	f_oE	$\Delta_{rel}(N_mE)$	$\Delta_{rel}(h_mE)$	$\Delta_{rel}(f_oE)$
Arecibo	1.21E+11	106.54	3.14	0.00	0.00	0.00
Low-resolution	1.14E+11	106.00	3.03	6.40	0.51	3.25
High-resolution	1.164E+11	107.00	3.07	4.06	0.43	2.05

[c] at 19 UTC

4.2 Comparison between AURIC and COSMIC-1 GPS RO

More than 850 individual ionospheric data profiles have been observed on February 9, 2012 by five of the six different COSMIC-1 micro satellites (one satellite (C003) was inactive during the whole day). On this day, satellite-1 (C001) mapped Earth's ionosphere 287 times on its orbital path between 00:41-23:57 UTC. Satellite-2 (C002) produced 179 profiles between 04:12-23:57 UTC. Satellite-4 (C004) observed 201 profiles from 00:07-23:55 UTC, satellite-5 (C005) observed 66 profiles from 00:26-23:46 UTC, and Satellite-6 (C006) observed 162 profiles from 00:01-23:40 UTC. All these observations correspond to different latitudes and longitudes.

We impose three constraints to select appropriate ionospheric EDPs for comparison between COSMIC-1 observations and AURIC model results. Criteria are listed below:

1. The time of the observed ionospheric data profile must coincide with daytime profiles (local solar time morning, noon, and/or afternoon).
2. We choose only those occultation profiles which have latitude coverage within $\pm 20^{\circ}$ and longitude coverage within $\pm 30^{\circ}$ of Arecibo and Millstone Hills to understand the latitudinal effect of radio occultations. Also, lower atmosphere (below E-region) and upper atmosphere (F-1 region and above) condition would be similar for a single observation and seasonal effect on ionospheric EDPs would be same.
3. No negative electron density above 100 km, and the altitude range of the observations must not have a data gap within E-region altitudes ($\sim$ 90 - 150 km) .

Our analysis of COSMIC-1 is limited from 100 km to 150 km. Below 100 km, we found that some of the profiles carry negative electron density values. These misleading values may occur in the electron density profiles due to standard Abel inversion of the satellite radio signal (more detail of this technique can be found in the work by Hajj & Romans, 1998, and references there in) that assumes spherical symmetry (vertical electron density gradient only). Validation and error analysis of radio occultation data can be found in Schreiner et al. (1999). These negative values are the indication of the limitations of the profile retrievals if horizontal gradients are not considered in the inversion of occultation data (Lei et al., 2007). Mentioned earlier in section 2.1.3, Pedatella et al. (2015) also found that standard Abel inversion ion profiles produce larger errors in the E-region electron density measurements and proposed an improved inversion of electron

density profiles called gradient assisted ionospheric profiles ('igaPrf'). Up to date, UCAR had recently (Nov, 2022) published 'igaPrf' profiles and became publicly available. Additionally, COSMIC-1 observations do not coincide well during the chosen periods with Arecibo ISR and Millstone Hills ISR. As COSMIC-1 observations show the sparseness of data availability, it is impractical to compare these COSMIC-1 profiles with radar observations rather we can run our model in exact location of radio occultation profiles.

Figure 4 shows two radio occulation EDPs observed by COSMIC-1 in two different latitude (low and middle, respectively), longitude, and local solar time. Our comparison is consistent with the proposed hypothesis that the high-resolution cross section and solar irradiance produce more ionization at the E-region regardless the location or time. Specifically, left panel of Figure 4 shows the curve from COSMIC-1 (C001) orbit at 16.15 UT (9.80 Hr local solar time). Besides, we included another profile from COSMIC-1 (C005) (right panel of Figure 4) orbit at 12.22 UT (9.13 Hr local solar time). Our model setup is different for these two runs and updated high-resolution runs by AURIC are more aligned with data, as well as, producing more ionization than the low resolution runs.

4.3 Comparison between AURIC and empirical models

Two empirical models, IRI-2016 and FIRI-2018, are compared with AURIC model results at the location of Arecibo ISR observations, as can be seen in Figure 5. The IRI-2016 model (web-based version) incorporates several user required input parameters (see Table 2). Figure 5 presents the IRI-2016 predicted EDP as a function of altitude between $90-150$ km (dark green pentagon) with a 1 km step size over-plotted with the hourly averaged EDP from the Arecibo campaign at 16 UTC. All other input parameters of IRI-2016 are set as default.

FIRI-2018, an improved version of IRI for the lower ionosphere (Friedrich et al., 2018), is also included in that Figure 5. Here, we show the FIRI-2018 EDPs as a function of altitude (lime green star) from $90-150$ km. We also tabulated all the input parameters required for this empirical model in Table 2.

A quantitative comparison in terms of N_mE, h_mE and f_oE between the empirical models and AURIC is shown in Table 3. The IRI-2016 predicted EDP demonstrates differences of $\sim 13.39\%$, $\sim 0.28\%$ and $\sim 6.93\%$ in terms of peak electron density, peak height, and critical frequency (N_mE, h_mE, and f_oE) with the high-resolution AURIC run, respectively, while the low-resolution model outputs show larger discrepancies. FIRI-2018 EDP shows small discrep-

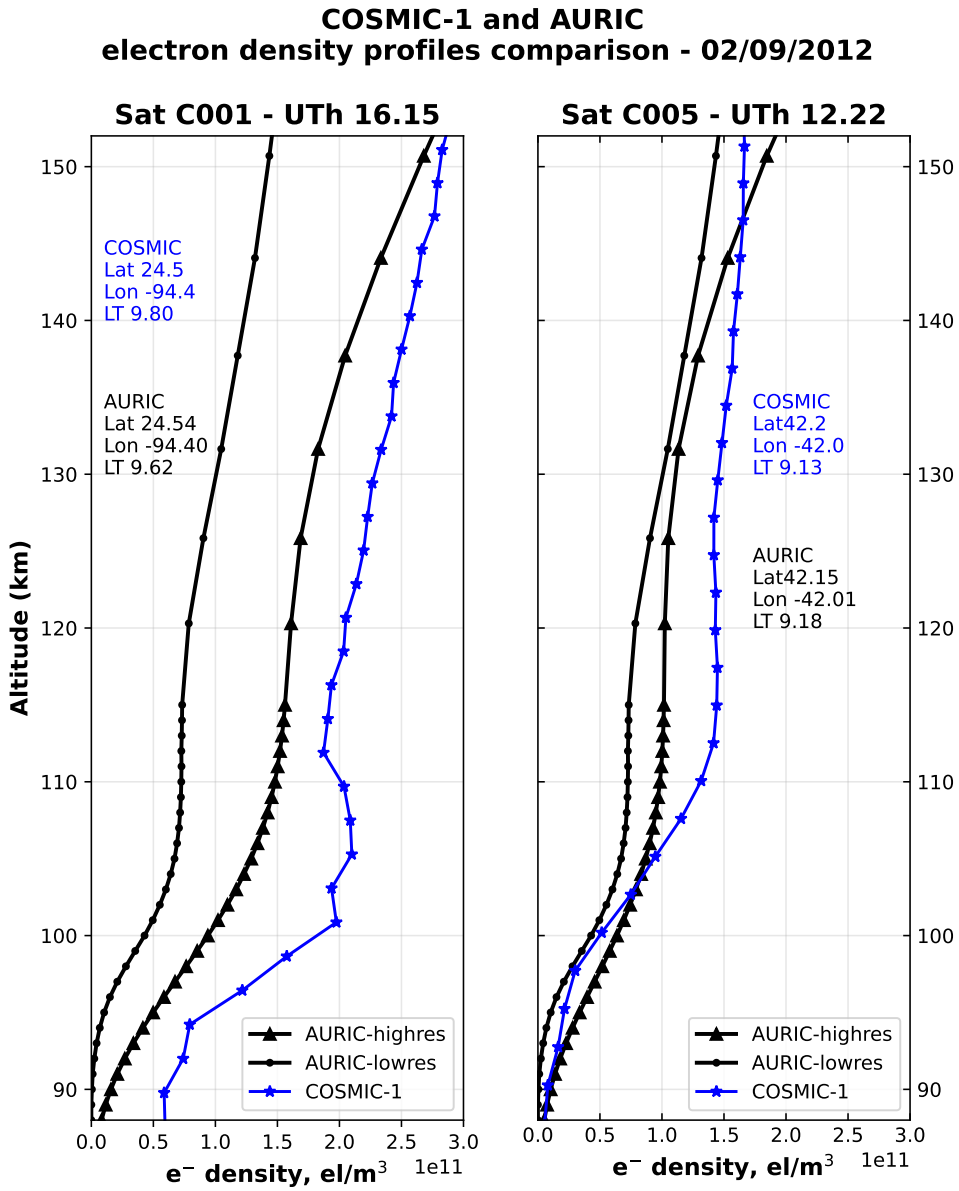

Figure 4. Comparison between observations by COSMIC-1 GPS RO profiles (blue star - iga profiles) with updated AURIC (black triangle - high-res, black circle - low-res) at the same location of radio occultations.

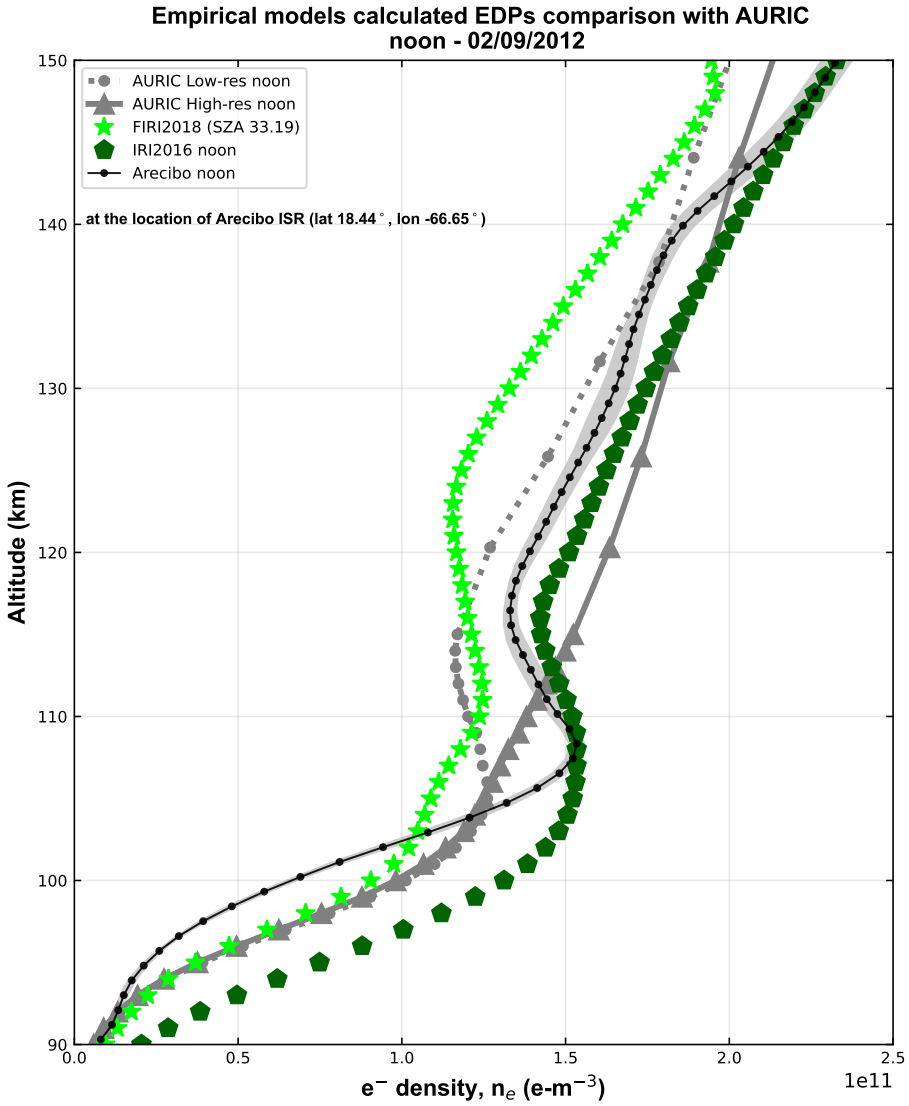

Figure 5. Comparison between empirical models (IRI-2016 (lime - triangle) and FIRI-2018 (sky blue - star)) with AURIC calculations (same as in Figure 4). Arecibo ISR observation (black circular solid line with shaded region as 1-σ standard deviation) at the noon time is also presented as a reference.

Table 2. Selected input parameters of empirical models

	IRI-2016	FIRI-2018
Date	February 9, 2012	40 (J. Day)
Time (UTh)	16	33.19 (SZA)
Latitude (degree)	18.44° N	18.34° N
Longitude (degree)	293.4°	-
Altitude (km)	90-180	90-150
Stepsize (km)	1	1
Sunspot number	66.9	-
F10.7 radio flux (daily) (s.f.u.)	99.2	-
F10.7 radio flux (81-day) (s.f.u.)	115.1	-
Ionospheric index (IG12)	78.2	-

J = Julian; SZA = Solar Zenith Angle

ancy with the high-resolution model outputs in terms of N_mE and f_oE ($\sim 6.01\%$ and $\sim 3.35\%$, respectively). The low-resolution model is more consistent with FIRI-2018 having less discrepancy than the high-resolution model. Perhaps the better agreement with low-resolution AURIC output is because FIRI-2018 also uses low-resolution cross sections (0.02 nm) of O_2 for Lyman-α (Carver et al., 1977) reported by Friedrich and Torkar (2001).

4.4 Comparison between AURIC and Millstone Hills (MLH) ISR

The Millstone Hills ISR data set contains three hours of electron density vertical profiles during afternoon time only (18-19 Hr, 19-20 Hr, 20-21 Hr UTC) from just above $\sim$ 95 km to $\sim$ 1000 km. The left panel of Figure 6 shows individual 12 profiles of MLH alternating code (AC) data between 18-19 Hr UTC (slate blue color) with ~ 4 min cadence and altitudes ranging from ~ 96 km up to ~ 150 km. The corresponding mean profile with observational uncertainty (standard deviation) at 18-19 UTC is also shown in Figure 6 (dark navy blue with shaded region as error). This plot demonstrates a peak electron density with values of $1.264\times10^{11}\ m^{-3}$ at a height of 110.2 km. Similarly, the right panel of this Figure 6 demonstrates 15 profiles recorded in one hour later i.e., 19-20 Hr UTC (light red) with the corresponding mean and standard deviation of the profiles shown as a brown diamond dotted line with shaded region as uncertainty.

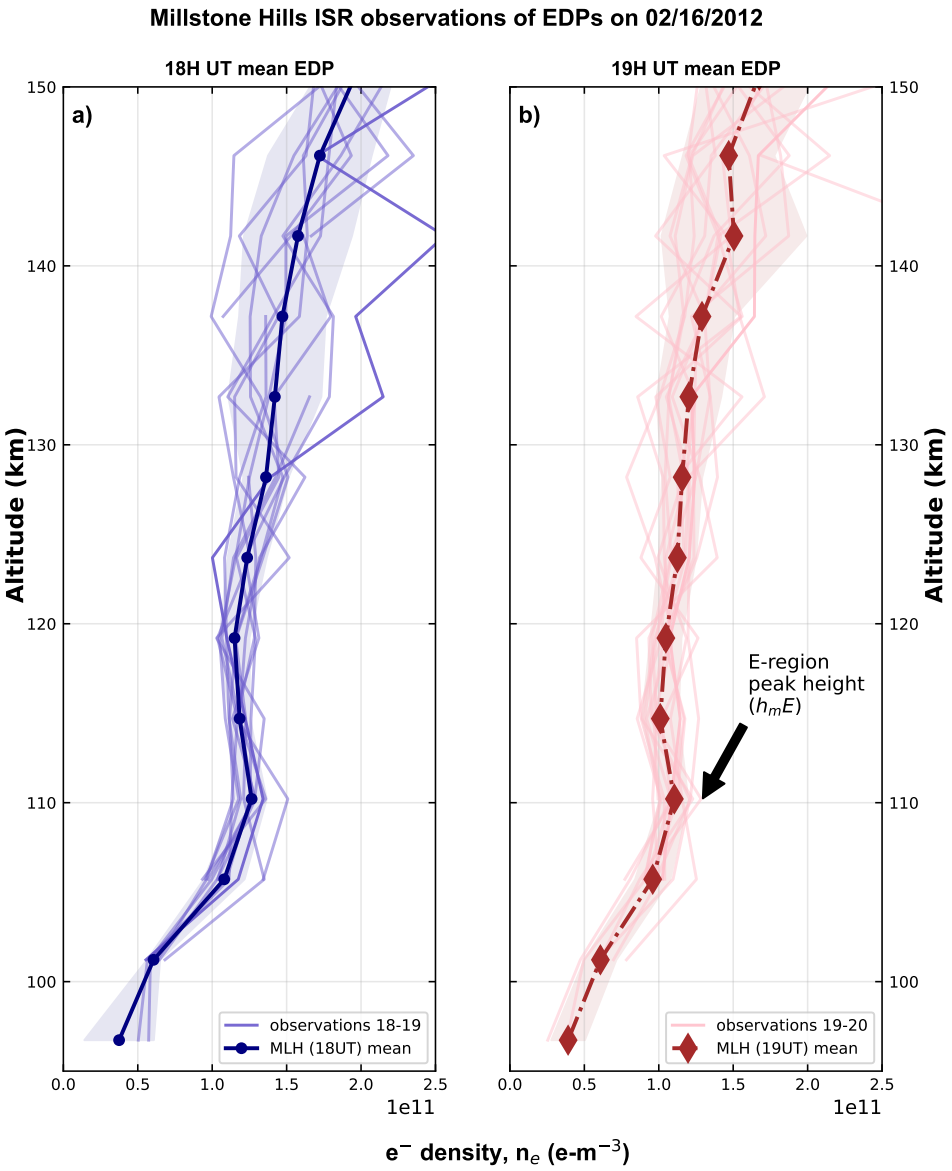

Figure 6. Millstone Hills ISR (42.61°N, 288.5°E) electron density observation with associated uncertainty as a function of altitude at 18 UTC (left panel) and 19 UTC (right panel) on February 16, 2012.

Table 3. Quantitative Comparison between empirical models and AURIC

Noon[e]	N_mE (e^-/m^3)	h_mE (km)	f_oE (MHz)	$\Delta_{rel}(N_mE)$ (%)	$\Delta_{rel}(h_mE)$ (%)	$\Delta_{rel}(f_oE)$ (%)
IRI-2016	1.53E+11	108.30	3.52	0.00	0.00	0.00
Low-resolution	see Table 1[b]	see Table 1[b]	see Table 1[b]	17.58	3.05	9.21
High-resolution	”	”	”	13.39	0.28	6.93
[e] at 16 UTC						
Noon[f]	N_mE (e^-/m^3)	h_mE (km)	f_oE (MHz)	$\Delta_{rel}(N_mE)$ (%)	$\Delta_{rel}(h_mE)$ (%)	$\Delta_{rel}(f_oE)$ (%)
FIRI-2018	1.25E+11	111.00	3.17	0.00	0.00	0.00
Low-resolution	see Table 1[b]	see Table 1[b]	see Table 1[b]	0.88	5.41	0.82
High-resolution	”	”	”	6.01	2.70	3.35
[f] SZA = 33.19°						

Table 4. Quantitative Comparison between MLH ISR and AURIC

Afternoon[g]	N_mE (e^-/m^3)	h_mE (km)	f_oE (MHz)	$\Delta_{rel}(N_mE)$ (%)	$\Delta_{rel}(h_mE)$ (%)	$\Delta_{rel}(f_oE)$ (%)
MLH	1.10E+11	110.21	2.99	0.00	0.00	0.00
Low-resolution	9.37E+10	108.00	2.76	15.13	2.01	7.88
High-resolution	9.51E+10	110	2.78	13.89	0.19	7.20
[g] at 19 UTC						

While the E-region peak height (h_mE) remains unchanged (110.2 km), the N_mE has slightly decreased ($1.105\times10^{11}\ m^{-3}$) in comparison to profiles from the previous hour. This is expected as the Sun moves closer to the horizon and thus the solar radiation decreases. We compare the mean 19 Hr peak electron density value, peak height and calculated peak critical frequency with AURIC model results in Table 4. Figure 7 shows comparison of 19 UTC Millstone Hills ISR EDPs (brown diamonds dotted line) with AURIC. It is evident that AURIC prediction with high-resolution input at 19 Hr almost coincides with observation in between $\sim$ 115 km to $\sim$ 135 km. Clearly, the new AURIC calculation with high-resolution cross section inputs generates more realistic output than the low-resolution AURIC calculation.

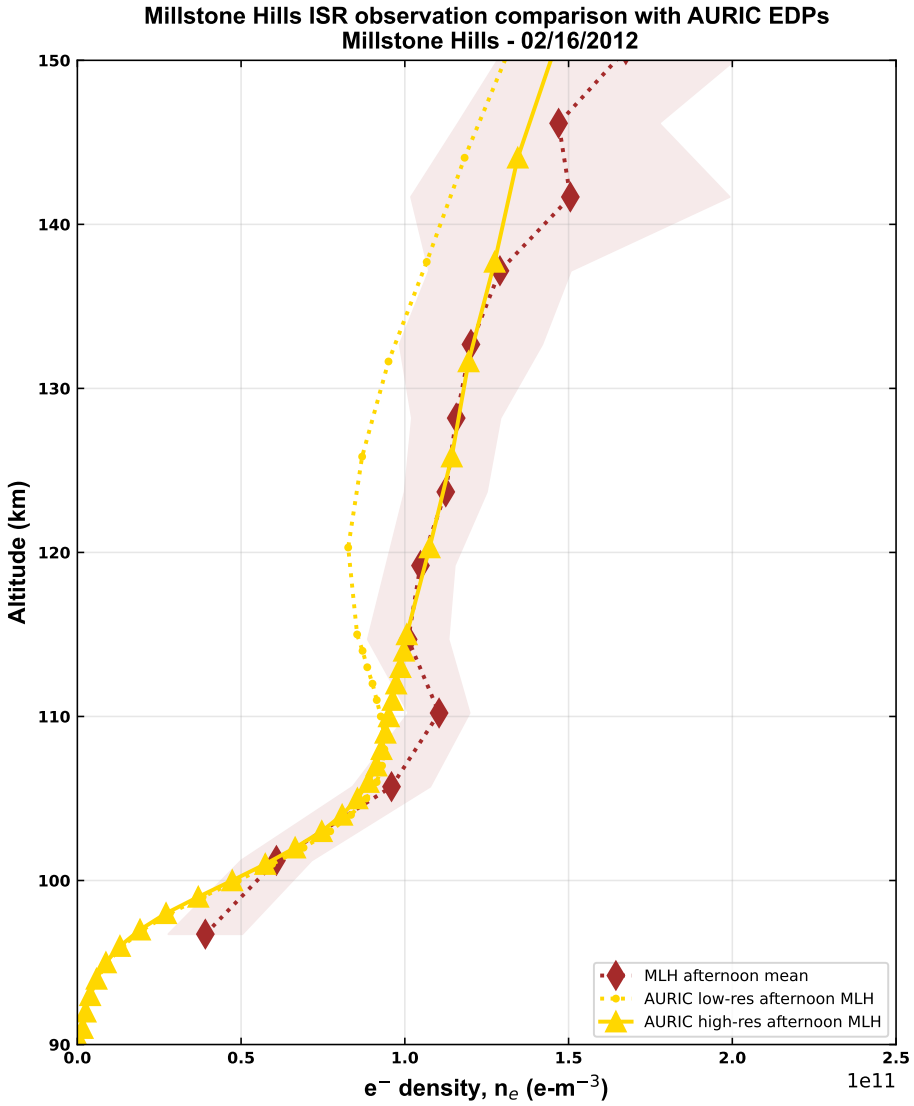

Figure 7. Comparison between Millstone Hills ISR observations (brown diamond dotted line) at 19 UTC with corresponding AURIC runs using the low-resolution (circular dotted) and the high-resolution (triangle solid) cross sections on February 16, 2012.

Relative percent difference between MLH ISR and AURIC model is in better agreement in terms of N_mE and f_oE when we use the high-resolution cross section (13.89% and 7.20%, discrepancy, respectively) than the low-resolution cross section as AURIC input (15.13% and 7.88%, respectively). Peak height of E-region EDP in the low-resolution AURIC run is close to the observation ($\sim 2\%$).

5 Discussion

As the photon flux from the Sun to the atmosphere varies with altitude, local time, location and season, so do the EDPs in the E-layer (E. Appleton & Lyon, 1961; E. Appleton, 1963; Chu et al., 2009), and N_mE varies accordingly. Both solar and magnetic activity strongly influence the magnitude and variability of electron densities at all ionospheric altitudes. The geomagnetic and solar indices and radiative effects for the whole month of February 2012 are shown in Figure 1. Planetary Kp index is lower (~ 2) for both days and the derived daily average of the Ap index is also lower for February 9 and 16, (5 and ~ 4, respectively). These suggest that magnetic activity does not affect the EDP variations to a significant degree on our observational days. Similarly, the F10.7 radio flux values of ~ 99 and ~ 103 s.f.u for those days are also an indication of relatively quiet solar activity. The number of sunspots are relatively small (28 and 48) and there are no indications of any Earth directed coronal mass ejection or large class (X, M) solar flare eruptions from the Sun on those observational days measured by two other important ionospheric and thermospheric indices, which characterize the space weather and near-Earth space environmental conditions are the Dst (Disturbance storm-time) index and soft x-rays (SXRs) observation (λ ~1-8Å). We used these two indices for the month of February 2012 in addition to $K_p, A_p, F_{10.7}$ and number of sunspots. Detailed study of solar soft x-rays including background, origin, long term variability, and periodicity of SXR can be found in (Aschwanden, 1994). Data source for GOES X-ray is NOAA Space Weather Prediction Center (SWPC) and we have utilized GOES-15 level 2 X-ray sensor 1-minute irradiance average. The hourly equatorial Dst index is taken from the World Data Center for Geomagnetism, Kyoto, Japan. In February 2012, the mean Dst index was mostly between 0 to -25 nT except on 15th February, 2012 when it was ~ -55 nT (see Figure 1 panel (f)). Thus, the geomagnetic conditions were overall quiescent during the observed period. In Figure 1 panel (e), we included the X-ray observation (longer wavelength channel) by GOES satellite where it is clearly seen that X-ray flux always stays below 10^{-5} W/m^2 except on 6th, 7th, and 11th February, 2012. In those days, the flux values are slightly above 10^{-5} W/m^2 which indicates an M-class flare activity. But, during our observation time, C-class

411 flare activity had been observed (i.e., 9th and 16th February, 2012, the x-ray flux is just above
412 10^{-6} W/m^2 and just below 10^{-6} W/m^2, respectively.) Overall, solar and geomagnetic conditions
413 during the days of observation were relatively low and both days have similar solar and geomag-
414 netic conditions.

415 In any ionospheric radiative transfer model, such as AURIC, three inputs should be con-
416 sidered to calculate accurate results. These are : (1) Solar X ray and EUV irradiance (XUV all
417 together) input, (2) Cross sections (photoabsorption + photoionization), and (3) neutral compo-
418 sition and density as a function of altitude. In this paper, we selected two specific days (Febru-
419 ary 9 and 16, 2012) when space weather was calm.

420 In AURIC, we can vary the solar irradiance input as per the space weather condition. For
421 example, during high solar flare activity, the solar irradiance would be higher, which would al-
422 low more XUV flux into the upper atmosphere and therefore, produce more ionization than the
423 quiet time. So, theoretically, we should get more appropriate results from AURIC if we can set
424 the correct EUV and X-ray irradiance to the model along with other inputs during high solar ac-
425 tivity. But this paper is only evaluating the contribution of high-resolution cross sections keep-
426 ing the solar irradiance fixed, and that is the reason we choose those two specific days when the
427 sun is relatively quieter than the active time. Overall, by setting the correct solar irradiance and
428 high-resolution cross sections in AURIC, in principal, we can generate the correct EDP profiles
429 from AURIC even if it is not solar minimum condition.

430 Bulk of ionospheric measurement is too slow to gain any insight about quick changes in
431 ionosphere (Meier et al., 2002). In order to test the model output in terms of electron density ver-
432 tical profiles after employing certain updates such as high resolution photoionization and pho-
433 toabsorption cross sections of two important atmospheric constituent N_2 and O, as well as, high-
434 resolution solar spectrum (see Soto et al., 2023, for more detail), we simply use a single day anal-
435 ysis to understand the E-region variability in daily manner. Sojka et al. (2014) studied Arecibo
436 region E-layer with Arecibo ISR data campaign on February 9, 2012 and two of ionospheric mod-
437 els incorporated high-resolution solar irradiance by Solar Dynamic Observatory (SDO) onboard
438 Extreme Ultraviolet Variability Experiment (EVE). Our study utilize the same dateset. Figure
439 2 shows the daily variability of electron density peak absolute value and height at E-region in a
440 single day Arecibo ISR observation exactly same like Sojka et al. (2014). Uncertainty analysis
441 and data variation can also be found in Sojka et al. (2014). On the other hand, Millstone hills ISR
442 is located in different latitude and EDP measured on February 16, 2012. To compare with AU-
443 RIC model data, we measured the hourly mean values from all ISR observations to keep local

time fixed and measured 1-σ standard deviation at each altitude step to predict the measurement error. AURIC simulations presented in paper for Arecibo and Millstone comparison are in two different latitudes and two entirely different model setup.

AURIC predicts less ionization than data during early-morning regardless of the cross section inputs to the model (blue and cyan profiles in Figure 3). During noon (black and grey profiles) and afternoon (red and majenta profiles in Figure 3), the model calculations show similar trends from ~ 90 km to ~ 105 km. Clearly, new high-resolution cross section calculations with a new high-resolution solar spectrum model produces a higher rate of photoionization, which is more distinctive above ~ 105 km to ~ 110 km. This specific altitude range is important, as the E-region peak electron density is usually located in this range. The peak at the E-region is not clearly detected in the new high resolution AURIC calculations. Therefore, we compare the model electron density value using the altitude of the real time h_mE observed by Arecibo ISR.

Two empirical models have been used in the study to compare with AURIC outputs. Generally, Thermosphere and Ionosphere models are of two kinds, first, physics based models, such as AURIC, GLOW, and various general circulation models, etc., and the second kind is empirical/semi-empirical models such as IRI, FIRI. IRI-2016 is an empirical model which does not use any existing theoretical approach for understanding ionospheric processes rather it is using real-time data from ground and space-based observations such as rocket sondes, radars, and more recently satellites. On the other hand, FIRI-2018 is a semi-empirical model, which is a combination of data and an ion-chemical model, specifically, using an analytical function for the lower ionosphere and neutral atmosphere and output is adjusted by a limited number of rocket measurements. Friedrich et al. (2018) mentioned two important limitations in the FIRI-2018 model. First, the use of obsolete solar flux measurements (Delaboudinière et al., 1978; Manson, 1976), and, second, absorption and ionization cross sections used in the model pose insufficient or lower resolution. Therefore, FIRI is very good for D-region electron density analysis, but perhaps, not precise for E-region EDP calculation as solar X-rays and EUV absorbs in E-region and it is required to have both high-resolution calculation and observations. Due to the differences in the underlying assumptions, mathematical formulations, and the amount of data assimilated, a certain degree of difference is natural among the different models. Especially, the theoretical models and empirical models are naturally very different, however, they empirical models are thought to capture the average (or typical) behavior of the atmosphere-ionosphere, therefore they are commonly used to validate theoretical models. In our comparison, it is evident that AURIC with N_2 and O high resolution

cross sections and high-resolution solar irradiance profile is much better aligned with IRI-2016 and the Arecibo radar profiles, which is a major improvement in a physics-based model.

Figures 3,4,5, and 7 confirm our hypothesis that high resolution absorption and ionization cross sections allow the penetration of much more solar EUV radiation into the E and D regions than is allowed by low-resolution cross sections (at a fixed location and time, the high -resolution cross section AURIC produces $\sim$ 10% more electrons than the low resolution run at 110 km, while at 120 km, the discrepancy rises to $\sim 22\%$). However, electron densities computed from the high-resolution transmission do not agree in shape with the observations. There are several possible reasons for this discrepancy.

The photoionization rate around 120 km is controlled principally by two factors: the passage of light through N_2 and O_2 molecular bands longward of 80 nm and the O_2 photoionization cross section (Soto et al., 2023). The O_2 bands are broadened in this region by predissociation and can be spectrally resolved and measured accurately in the laboratory, so we do not consider them a source of uncertainty. On the other hand, N_2 bands consist of a very large number of rotational lines that are not resolvable in the laboratory, so they must be modeled. Even with our model resolution of 0.001 nm, the spectral resolution is insufficient to reproduce the rotational line shapes, so the atmospheric transmission will only capture some of the peaks and valleys between the rotational lines. Although this has a direct effect on the photoionization rate of O_2 at 120 km, our preliminary calculations indicate that any error resulting from 0.001 nm resolution is very small (less than 0.5%). A major redesign of AURIC is not within the scope of this work, thought we hope to investigate this effect in the future.

Currently we compute the O_2 photoionization rate using the cross section from the Conway (1988) compilation, which is traceable to the laboratory measurements of Samson et al. (1977, 1982). Their measurements are not sufficient to resolve autoionization lines that play a significant role in the penetration of solar EUV radiation to the lower ionosphere (Meier et al., 2007; Soto et al., 2023). It is possible that new theoretical calculations of the O_2 cross section will improve the agreement between the models and observations in Figures 3,4,5, and 7. Finally, the AURIC model does not include diffusion or dynamics, which have the potential to alter the altitude profiles. Investigation of these effects will be addressed in a future analysis.

Besides, Figure 8 shows a contribution plot of AURIC volume production rates (VPRs) as a function of altitude for February 9, 2012 at noon for four different flavours of AURIC. Volume production rates for the dominant three states of O, N_2, and O_2 and a pseudo state for O (con-

taining the VPR contribution for 29 states) are shown as color-coded symbols (see legend) along with corresponding model EDP (dashed black line) and Arecibo observatory ISR EDP with measurement uncertainty (purple line). The total VPR are the orange circles. Panel (A) shows the AURIC model calculations utilizing the new high-resolution (0.001 nm) O and N_2 photoionization and photoabsorption cross sections and Conway (1988) O_2 cross section interpolated onto the high-resolution grid. Panel (B) illustrates the model results using the new cross sections binned onto a low-resolution grid (0.05 nm resolution from 0.1-10 nm and 0.1 nm resolution from 10-105 nm) and the Conway (1988) O_2 cross section on the low-resolution grid. Panel (C) shows the model results utilizing the Conway (1988) cross section compilation interpolated onto a high-resolution (0.001 nm) grid and panel (D) illustrates model results using the Conway (1988) compilation cross sections on the low-resolution grid. In the paper, "high-resolution" AURIC run corresponds panel (A) and "low-resolution" AURIC run corresponds panel (D).

Indeed, the shape and magnitude of the $O_2^+(X)$ is the main contributor at lower altitude. However, in Panel A (new high resolution model results) we see increased $O^+(4So)$ VPR extending down to about 110 km which is different from the other cases.

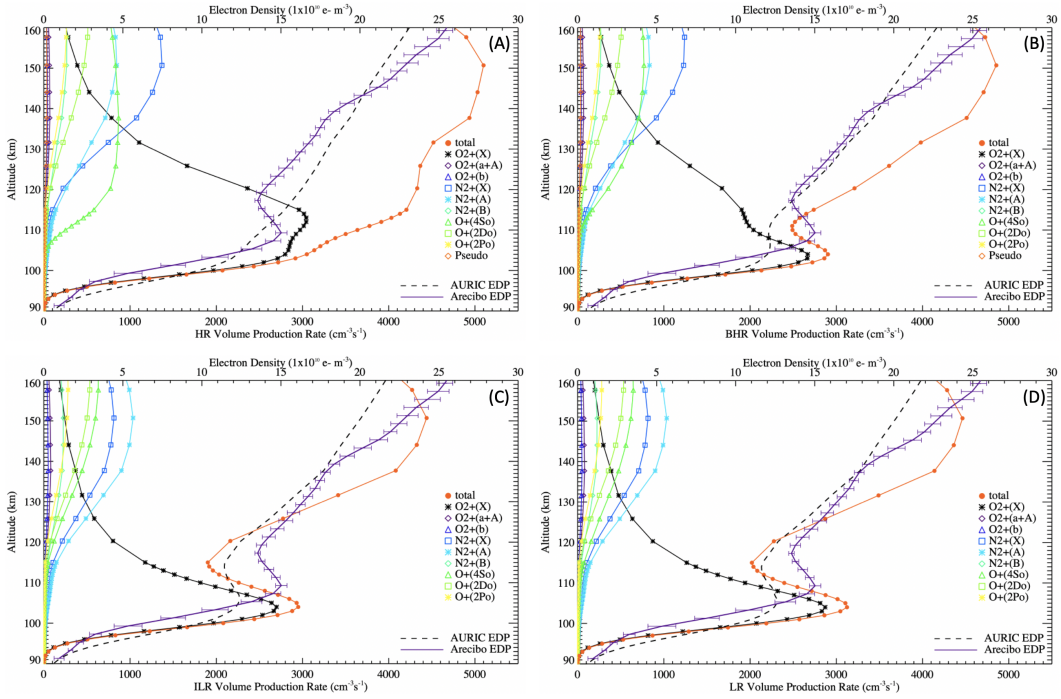

Figure 8. AURIC volume production rates vs altitude for February 9, 2012 16UTC (noon) are shown with the corresponding AURIC model EDP (dashed black line) and Arecibo Observatory ISR EDP with 1-sigma uncertainties (purple line).

6 Summary and Conclusion

AURIC calculations of varying flavors (i.e., different sets of photoionization and photoabsorption cross sections and solar EUV spectrum) are used to calculate the ion composition that leads to the calculation of electron density in the E-region. This study presents a summary of daily ionospheric electron number density observations by several methods, including two incoherent scatter radars, one satellite system, and two empirical models for a solar quiet day. We compare measured electron densities with the output of AURIC using two different inputs: high-resolution cross sections and solar spectral irradiance; and low-resolution cross sections. The main focus of this study is to take the first step and compare the real time EDPs with the output of a simplified model of the E-region using new calculations of high resolution cross sections and solar spectral irradiance.

It is evident that modeled E-region electron densities are significantly increased with the high resolution cross sections and are likely to account for the mismatch between earlier models and the data. Incorporating high-resolution cross section calculations in the AURIC model clearly increases the photoionization rate and therefore the electron density in the E-region, improving agreement with observations by radars, satellites, and empirical model calculations. However, the altitude profiles of the high resolution model EDPs do not generally agree with the data in terms of peak density. Future investigation of this work should address the inclusion of molecular oxygen (O_2) high-resolution calculation of photoabsorption and photoionization cross sections in the model that may improve the agreement between observed and modeled E-region electron density profile shapes. Nevertheless, inter comparison between AURIC and other ionosphere models could well identify differences in physics, such as dynamics that could account for the mismatch with the data. Overall, considering all the uncertainties involved in calculation and data analysis discussed above, during a solar quiet day the simulated high-resolution version of AURIC and measured electron density vertical profiles are more aligned than the low-resolution AURIC runs.

Appendix A : Physics of photoionization

Absorption of photons at a certain wavelength (i.e., short wavelength; high frequency) by a neutral atom causes the ejection of an electron, therefore, ions-electrons pairs form at the upper atmosphere of the Earth. It's called photoionization. E-region ionization occurs primarily by solar extreme ultraviolet photons (EUV) and X-rays at certain energy ranges when λ (wavelength) < 100 nm. Following Meier et al. (2007), The photoionization rate (j) can be defined as the product of ionization frequency (g) and number density (n) of the species (i). Mathematically,

$$j_i(z) = g_i(z) * n_i(z) \tag{A1}$$

Unit of photoionization rate (j) is ionization $cm^{-3}s^{-1}$ if ionization frequency (g) can be expressed as unit of s^{-1} and number density (n) is expressed as a unit of cm^{-3}. The ionization frequency (g) at high spectral resolution can be expressed as,

$$g_i(z) = \int_0^{\lambda_i^t} \sigma_i(\lambda) F_s(\lambda) e^{-\tau(z,\lambda)} d\lambda \tag{A2}$$

where, σ is the threshold wavelength photoionization cross section of the species (i), F_s is the solar spectral irradiance (unit: photons $cm^{-2}s^{-1}nm^{-1}$) and τ is the optical depth (or optical thickness) at wavelength between the reference altitude altitude (z) and the Sun.

The optical depth (τ) can be defined as (Yiğit, 2018)

$$\tau(z,\lambda) = \sum_i \sigma_i^a(\lambda) \int_z^\infty n_i(z^{'}) ds, \tag{A3}$$

where a stands for total absorption and s is the distance along the path of the penetrating photons. For an overhead Sun, solar zenith angle must be 0° which satisfies $s = z^{'}$. The computation of ionization frequency is mostly carried out by mapping of cross sections and optical depths for species O, O_2, and N_2 respectively.

Appendix B : E-region critical frequency

Generally, an electromagnetic (EM) radio wave propagating from the ground to the ionosphere can be reflected by ionospheric layers, depending on the electron density profile. EM waves with a higher frequency will penetrate and propagate to relatively higher altitudes. The maximum frequency that can be reflected from the E-region layer (i.e., from $\sim$ 90 km up to $\sim$ 150 km) is called the E-region critical frequency (f_oE) which is proportional to the maximum electron density in the E-region (N_mE). The corresponding height of the peak E-region electron density

is denoted by h_mE. Photoelectrons are those that are at much higher than thermal energies, typically around 1-100 eV, produced in the E-region oscillate in response to the time varying electric field and can be described by the plasma frequency of electrons (ω_{p_e}). Following equation 2.6 from Schunk and Nagy (2009) or equation 8(a) from Unz (1963) modified for Thomson scatter radar observation (Evans, 1969; Semeter, 2020), we can express the critical frequency that refers to the location at which maximum refraction occurs, and the height where we find the maximum electron density, in functional form:

$$f_oE = \frac{1}{2\pi}\sqrt{\left(\frac{n_e * e^2}{\epsilon_0 * m_e}\right)} \approx 8.98\sqrt{n_e} \approx 9\sqrt{n_e}, \tag{B1}$$

where, $n_e = N_mE$ is the maximum electron density at the height of h_mE, ϵ_0 is the permittivity at free space, e is the electron charge and m_e is the mass of electron. All parameters must be expressed in SI units to evaluate Equation B1. Typically, for a summer day at low solar activity, this value can range from $2-4$ MHz and reach up to 6 MHz during high solar activity (Figure 1, Sheiner et al., 2020).

Acronyms

AURIC Atmospheric Ultraviolet Radiance Integrated Code

COSMIC Constellation observing system for meteorology ionosphere and climate

COSPER Committee on Space Research

C/NOFS-CINDI Communications/Navigation Outage Forecasting System - Coupled Ion-Neutral Dynamics Investigation

EDP Electron density profile

GLOW model GLobal AirglOW model

ISR Incoherent scatter radar

IRI International Reference Ionosphere

MLH Millstone Hills

RO Radio occultation

SDO-EVE Solar Dynamics Observatory - Extreme Ultraviolet Variability Experiment

UCAR University Corporation for Atmospheric Research

URSI International Union of Radio Science

Acknowledgments

The Arecibo Observatory is the principal facility of the National Astronomy and Ionosphere Center, which is operated by Cornell University under a cooperative agreement with the National Science Foundation (NSF). We appreciate Millstone Hills radar observatory and COSMIC-1 team for making their data publicly available. We also want to thank IRI and FIRI model development team for making their model available online. Additionally, we thank two reviewers for helpful comments and suggestions. This material is based upon work supported by the National Science Foundation under Grant No. 1849014.

Data availibility statement

AURIC model outputs, Observational data from Arecibo ISR, COSMIC-1, IRI-2016, FIRI-2108, Millstone Hills ISR, and associated code needed to read the data files are publicly available on Zenodo (Sakib et al., 2023).

References

Anderson, D., Forbes, J., & Codrescu, M. (1989). A fully analytic, low-and middle-latitude ionospheric model. *Journal of Geophysical Research: Space Physics*, *94*(A2), 1520–1524.

Anthes, R. A., Bernhardt, P., Chen, Y., Cucurull, L., Dymond, K., Ector, D., ... others (2008). The cosmic/formosat-3 mission: Early results. *Bulletin of the American Meteorological Society*, *89*(3), 313–334.

Appleton, E. (1963). A seasonal anomaly in the ionospheric e-layer. *Journal of Atmospheric and Terrestrial Physics*, *25*(10), 577–579.

Appleton, E., & Lyon, A. (1961). Studies of the e-layer of the ionosphere—ii: Electromagnetic perturbations and other anomalies. *Journal of Atmospheric and Terrestrial Physics*, *21*(2-3), 73–99.

Appleton, E. V., & Barnett, M. A. F. (1925). Local reflection of wireless waves from the upper atmosphere. *Nature*, *115*(2888), 333–334.

Aschwanden, M. J. (1994). Irradiance observations of the 1–8 å solar soft x-ray flux from goes. *Solar Physics*, *152*, 53–59.

Bailey, S. M., Barth, C. A., & Solomon, S. C. (2002). A model of nitric oxide in the lower thermosphere. *Journal of Geophysical Research: Space Physics*, *107*(A8), SIA–22.

Bartels, J. (1949). The standardized index, ks, and the planetary index, kp. *IATME Bull*, *97*(12b), 0001.

Bartels, J. (1957). The geomagnetic measures for the time-variations of solar corpuscular radiation, described for use in correlation studies in other geophysical fields. *Ann. Intern. Geophys.*, *4*, 227–236.

Bell, K., & Stafford, R. (1992). Photoionization cross-sections for atomic oxygen. *Planetary and space science*, *40*(10), 1419–1424.

Berk, A., Bernstein, L. S., & Robertson, D. C. (1987). *Modtran: A moderate resolution model for lowtran* (Tech. Rep.). Spectral Sciences Inc Burlington MA.

Bilitza, D., Altadill, D., Truhlik, V., Shubin, V., Galkin, I., Reinisch, B., & Huang, X. (2017). International reference ionosphere 2016: From ionospheric climate to real-time weather predictions. *Space weather*, *15*(2), 418–429.

Bilitza, D., Pezzopane, M., Truhlik, V., Altadill, D., Reinisch, B. W., & Pignalberi, A. (2022). The international reference ionosphere model: A review and description of an ionospheric benchmark. *Reviews of Geophysics*, e2022RG000792.

Bilitza, D., Rawer, K., Bossy, L., & Gulyaeva, T. (1993). International reference ionosphere—past, present, and future: I. electron density. *Advances in Space Research*, *13*(3), 3–13.

Brown, S., Bilitza, D., & Yiğit, E. (2018). Ionosonde-based indices for improved representation of solar cycle variation in the international reference ionosphere model. *Journal of Atmospheric and Solar-Terrestrial Physics*, *171*, 137–146.

Carver, J. H., Gies, H., Hobbs, T., Lewis, B., & McCoy, D. (1977). Temperature dependence of the molecular oxygen photoabsorption cross section near the h lyman α line. *Journal of Geophysical Research*, *82*(13), 1955–1960.

Chu, Y.-H., Wu, K.-H., & Su, C.-L. (2009). A new aspect of ionospheric e region electron density morphology. *Journal of Geophysical Research: Space Physics*, *114*(A12).

Clette, F., & Lefèvre, L. (2016). The new sunspot number: assembling all corrections. *Solar Physics*, *291*(9), 2629–2651.

Conway, R. R. (1988). *Photoabsorption and photoionization cross sections of o, o2, and n2 for photoelectron production calculations: A compilation of recent laboratory measurements.* (Tech. Rep.). NAVAL RESEARCH LAB WASHINGTON DC. Retrieved from `https://apps.dtic.mil/sti/pdfs/ADA193866.pdf`

Delaboudinière, J.-P., Donnelly, R., Hinteregger, H., Schidtke, G., & Simon, P. (1978). *Intercomparison/compilation of relevant solar flux data related to aeronomy (solar cycle 20); cospar technique manual 7.*

Evans, J. V. (1969). Theory and practice of ionosphere study by thomson scatter radar. *Proceedings of the IEEE*, *57*(4), 496–530.

Friedrich, M., Pock, C., & Torkar, K. (2018). Firi-2018, an updated empirical model of the lower ionosphere. *Journal of Geophysical Research: Space Physics*, *123*(8), 6737–6751.

Friedrich, M., & Torkar, K. (2001). Firi: A semiempirical model of the lower ionosphere. *Journal of Geophysical Research: Space Physics*, *106*(A10), 21409–21418.

Gustafsson, G., Papitashvili, N., & Papitashvili, V. (1992). A revised corrected geomagnetic coordinate system for epochs 1985 and 1990. *Journal of atmospheric and terrestrial physics*, *54*(11-12), 1609–1631.

Hajj, G. A., & Romans, L. J. (1998). Ionospheric electron density profiles obtained with the global positioning system: Results from the gps/met experiment. *Radio Science*, *33*(1), 175–190.

Hedin, A. E. (1991). Extension of the msis thermosphere model into the middle and lower atmosphere. *Journal of Geophysical Research: Space Physics*, *96*(A2), 1159–1172.

Hinteregger, H. E., Fukui, K., & Gilson, B. R. (1981). Observational, reference and model data on solar euv, from measurements on ae-e. *Geophysical Research Letters*, *8*(11), 1147–1150.

Lai, P.-C., Burke, W. J., & Gentile, L. (2013). Topside electron density profiles observed at low latitudes by cosmic and compared with in situ ion densities measured by c/nofs. *Journal of Geophysical Research: Space Physics*, *118*(5), 2670–2680.

Lean, J., Woods, T., Eparvier, F., Meier, R., Strickland, D., Correira, J., & Evans, J. (2011). Solar extreme ultraviolet irradiance: Present, past, and future. *Journal of Geophysical Research: Space Physics*, *116*(A1).

Lean, J. L., Coddington, O., Marchenko, S. V., Machol, J., DeLand, M. T., & Kopp, G. (2020, August). Solar Irradiance Variability: Modeling the Measurements. *Earth and Space Science*, *7*, 00645. doi: 10.1029/2019EA000645

Lean, J. L., Warren, H. P., Mariska, J. T., & Bishop, J. (2003, February). A new model of solar EUV irradiance variability 2. Comparisons with empirical models and observations and implications for space weather. *Journal of Geophysical Research (Space Physics)*, *108*(A2), 1059. doi: 10.1029/2001JA009238

Lei, J., Liu, L., Wan, W., & Zhang, S.-R. (2005). Variations of electron density based on long-term incoherent scatter radar and ionosonde measurements over millstone hill. *Radio science*, *40*(2), 1–10.

Lei, J., Syndergaard, S., Burns, A. G., Solomon, S. C., Wang, W., Zeng, Z., ... others (2007). Comparison of cosmic ionospheric measurements with ground-based observations and model predictions: Preliminary results. *Journal of Geophysical Research: Space Physics*, *112*(A7).

Link, R., Strickland, D. J., & Daniell Jr, R. (1993). Auric airglow modules: Phase 1 development and application. In *Ultraviolet technology iv* (Vol. 1764, pp. 132–141).

Majeed, T., & Strickland, D. J. (1997). New survey of electron impact cross sections for photoelectron and auroral electron energy loss calculations. *Journal of Physical and Chemical Reference Data*, *26*(2), 335–349.

Manson, J. E. (1976). The solar extreme ultraviolet between 30 and 205 å on november 9, 1971, compared with previous measurements in this spectral region. *Journal of Geophysical Research*, *81*(10), 1629–1635.

Matzka, J., Stolle, C., Yamazaki, Y., Bronkalla, O., & Morschhauser, A. (2021). The geomagnetic kp index and derived indices of geomagnetic activity. *Space Weather*, *19*(5), e2020SW002641.

McGranaghan, R., Knipp, D. J., Solomon, S. C., & Fang, X. (2015). A fast, parameterized model of upper atmospheric ionization rates, chemistry, and conductivity. *Journal of Geophysical Research: Space Physics*, *120*(6), 4936–4949.

Meier, R., McLaughlin, B. M., Warren, H., & Bishop, J. (2007). Atomic oxygen photoionization rates computed with high resolution cross sections and solar fluxes. *Geophysical research letters*, *34*(1).

Meier, R., Warren, H., Nicholas, A., Bishop, J., Huba, J., Drob, D., ... others (2002). Ionospheric and dayglow responses to the radiative phase of the bastille day flare. *Geophysical research letters*, *29*(10), 99–1.

Pedatella, N., Yue, X., & Schreiner, W. (2015). An improved inversion for formosat-3/cosmic ionosphere electron density profiles. *Journal of Geophysical Research: Space Physics*, *120*(10), 8942–8953.

Prölss, G. (2012). *Physics of the earth's space environment: an introduction*. Springer Science & Business Media.

Rawer, K., Bilitza, D., & Ramakrishnan, S. (1978). Goals and status of the international reference ionosphere. *Reviews of geophysics*, *16*(2), 177–181.

Sakib, M. N., Soto, E., Yigit, E., Evans, J. S., & Meier, R. R. (2023, February). *Validation of E-region Model Electron Density Profiles using High-Resolution Cross Sections.* Zenodo [Dataset]. Retrieved from `https://doi.org/10.5281/zenodo.8117507` doi: 10.5281/zenodo.8117507

Samson, J. A., Gardner, J., & Haddad, G. (1977). Total and partial photoionization cross-sections of o2 from 100 to 800 å. *Journal of Electron Spectroscopy and Related Phenomena*, *12*(3), 281–292.

Samson, J. A., Rayborn, G. H., & Pareek, P. (1982). Dissociative photoionization cross sections of o2 from threshold to 120 å. *The Journal of Chemical Physics*, *76*(1), 393–397.

Schreiner, W. S., Sokolovskiy, S. V., Rocken, C., & Hunt, D. C. (1999). Analysis and validation of gps/met radio occultation data in the ionosphere. *Radio Science*, *34*(4), 949–966.

Schunk, R., & Nagy, A. (2009). *Ionospheres: physics, plasma physics, and chemistry*. Cam-

bridge university press.

Semeter, J. (2020). High-resolution approaches to ionospheric exploration. In *The dynamical ionosphere* (pp. 223–241). Elsevier.

Sharma, R., Brown, J., Berk, A., Acharya, P., & Gruninger, J. (1996). *User's manual for samm, sharc and modtran merged.* (Tech. Rep.). SPECTRAL SCIENCES INC BURLINGTON MA.

Sheiner, O., Rakhlin, A., Fridman, V., & Vybornov, F. (2020). New ionospheric index for space weather services. *Advances in Space Research*, *66*(6), 1415–1426.

Sheng, C., Deng, Y., Yue, X., & Huang, Y. (2014). Height-integrated pedersen conductivity in both e and f regions from cosmic observations. *Journal of Atmospheric and Solar-Terrestrial Physics*, *115*, 79–86.

Shiokawa, K., & Georgieva, K. (2021). A review of the scostep's 5-year scientific program varsiti—variability of the sun and its terrestrial impact. *Progress in Earth and Planetary Science*, *8*(1), 1–43.

Sojka, J. J., Jensen, J. B., David, M., Schunk, R. W., Woods, T., Eparvier, F., … Eccles, J. V. (2014). Ionospheric model-observation comparisons: E layer at arecibo incorporation of sdo-eve solar irradiances. *Journal of Geophysical Research: Space Physics*, *119*(5), 3844–3856.

Solomon, S. C. (2006). Numerical models of the e-region ionosphere. *Advances in Space Research*, *37*(5), 1031–1037.

Solomon, S. C., Hays, P. B., & Abreu, V. J. (1988). The auroral 6300 å emission: Observations and modeling. *Journal of Geophysical Research: Space Physics*, *93*(A9), 9867–9882.

Soto, E., Evans, J., Meier, R. R., Tashiro, M., Sakib, M. N., & Yiğit, E. (2023). A missing piece of the e-region puzzle: The need for high-resolution photoionization cross sections and solar irradiance in models. *JGR: Space Physics*. (Submitted)

Strickland, D., Bishop, J., Evans, J., Majeed, T., Shen, P., Cox, R., … Huffman, R. (1999). Atmospheric ultraviolet radiance integrated code (auric): Theory, software architecture, inputs, and selected results. *Journal of Quantitative Spectroscopy and Radiative Transfer*, *62*(6), 689–742.

Strickland, D. J., Evans, J. S., Bishop, J. E., Majeed, T., Shen, P. M., Link, R., & Huffman, R. E. (1996). Atmospheric ultraviolet radiance integrated code (auric): Current capabilities for rapidly modeling dayglow from the far uv to the near ir. In *Ultraviolet*

atmospheric and space remote sensing: Methods and instrumentation (Vol. 2831, pp. 184–199).

Tapping, K. (2013). The 10.7 cm solar radio flux (f10. 7). *Space weather*, *11*(7), 394–406.

Unz, H. (1963). The magneto-ionic theory for bound electrons. *Journal of Atmospheric and Terrestrial Physics*, *25*(5), 281–286.

Ward, W., Seppälä, A., Yiğit, E., Nakamura, T., Stolle, C., Laštovička, J., ... Pallamraju, D. (2021). Role Of the Sun and the Middle atmosphere/thermosphere/ionosphere In Climate (ROSMIC): a retrospective and prospective view. *Progress in Earth and Planetary Sciences*, *8*(1), 47. doi: 10.1186/s40645-021-00433-8

Warren, H. P. (2005). A solar minimum irradiance spectrum for wavelengths below 1200 å. *The Astrophysical Journal Supplement Series*, *157*(1), 147.

Woods, T. N., Eparvier, F. G., Hock, R., Jones, A. R., Woodraska, D., Judge, D., ... Viereck, R. (2012, January). Extreme Ultraviolet Variability Experiment (EVE) on the Solar Dynamics Observatory (SDO): Overview of Science Objectives, Instrument Design, Data Products, and Model Developments. *Solar Physics*, *275*(1-2), 115-143. doi: 10.1007/s11207-009-9487-6

Yan, R., Zhima, Z., Xiong, C., Shen, X., Huang, J., Guan, Y., ... Liu, C. (2020). Comparison of electron density and temperature from the cses satellite with other space-borne and ground-based observations. *Journal of Geophysical Research: Space Physics*, *125*(10), e2019JA027747.

Yiğit, E., & Medvedev, A. S. (2015). Internal wave coupling processes in earth's atmosphere. *Advances in Space Research*, *55*(4), 983–1003.

Yiğit, E., Knížová, P. K., Georgieva, K., & Ward, W. (2016). A review of vertical coupling in the atmosphere-ionosphere system: Effects of waves, sudden stratospheric warmings, space weather, and of solar activity. *J. Atmos. Sol.-Terr. Phys.*, *141*, 1–12. doi: http://dx.DOI.org/10.1016/j.jastp.2016.02.011

Yiğit, E. (2018). Planetary Ionospheres: Magnetic Fields, Chemical Processes, and Ionospheric Structure. In *Atmospheric and Space Sciences: Ionospheres and Plasma Environments* (pp. 67–102). Cham: Springer International Publishing. Retrieved 2022-02-15, from `http://link.springer.com/10.1007/978-3-319-62006-0_4` (Series Title: SpringerBriefs in Earth Sciences) doi: 10.1007/978-3-319-62006-0_4

Zhang, S.-R., Holt, J. M., & Kurdzo, J. (2011). Millstone hill isr observations of upper atmospheric long-term changes: Height dependency. *Journal of Geophysical Research:*

Space Physics, *116*(A2).